Cerebrovascular and blood-brain barrier impairments in Huntington's disease: Potential implications for its pathophysiology

[1]Janelle Drouin-Ouellet, PhD, [2]Stephen J. Sawiak, PhD, [3]Giulia Cisbani, PhD, [3]Marie Lagacé, MSc, [1]Wei-Li Kuan, PhD, [3]Martine Saint-Pierre, DEC, [4]Richard J. Dury, MSc, [3] Wael Alata, MSc, [3]Isabelle St-Amour, PhD, [1]Sarah L. Mason, PhD, [3,5]Frederic Calon, PhD, [3,6] Steve Lacroix, PhD, [4]Penny A. Gowland, PhD, [4]Susan T. Francis, PhD, [1]Roger A. Barker, MD, PhD and [3,7]Francesca Cicchetti, PhD

[1]Department of Clinical Neurosciences, John van Geest Centre for Brain Repair, University of Cambridge, Cambridge, CB2 0PY, United Kingdom; [2]Wolfson Brain Imaging Centre, Department of Clinical Neurosciences, University of Cambridge, Cambridge, United Kingdom; [3]Centre de recherche du CHU de Québec (CHUQ), Québec, QC, Canada G1V 4G2; [4]Sir Peter Mansfield Magnetic Resonance Centre, School of Physics and Astronomy, University of Nottingham, Nottingham, United Kingdom; [5]Faculté de Pharmacie, Université Laval, Québec, QC, Canada, G1V 0A6; [6]Département de Médecine Moléculaire, Université Laval, Québec, QC, Canada, G1V 0A6; [7]Département de Psychiatrie & Neurosciences, Université Laval, Québec, QC, Canada, G1V 0A6

Running Head: Vascular impairments in HD
Number of characters in the title: 123
Number of characters in the running head: 26
Number of words in the abstract: 247
Number of words in the body of the manuscript: 5127
Number of figures: 10
Number of color figures: 10
Number of tables: 2

Correspondence
Francesca Cicchetti, Ph.D.
Centre de recherche du CHU de Québec
Axe Neurosciences, T2-50
2705, Boulevard Laurier
Québec, QC, G1V 4G2, Canada
Tel #: (418) 656-4141 ext. 48853
Fax #: (418) 654-2753
E-mail: Francesca.Cicchetti@crchul.ulaval.ca

ABSTRACT

Objective: Although the underlying cause of Huntington's disease (HD) is well established, the actual pathophysiological processes involved remain to be fully elucidated. In other proteinopathies such as Alzheimer's and Parkinson's diseases, there is evidence for impairments of the cerebral vasculature as well as the blood-brain barrier (BBB), which have been suggested to contribute to their pathophysiology. We therefore investigated whether similar changes are also present in HD.

Methods: We used 3- and 7-Tesla magnetic resonance imaging as well as post-mortem tissue analyses to assess blood vessel impairments in HD patients. Our findings were further investigated in the R6/2 mouse model using *in situ* cerebral perfusion, histological analysis, Western blotting, as well as transmission and scanning electron microscopy.

Results: We found mutant huntingtin protein (mHtt) aggregates to be present in all major components of the neurovascular unit of both R6/2 mice and HD patients. This was accompanied by an increase in blood vessel density, a reduction in blood vessel diameter as well as BBB leakage in the striatum of R6/2 mice, which correlated with a reduced expression of tight junction-associated proteins (claudin-5 and occludin) and increased numbers of transcytotic vesicles, which occasionally contained mHtt aggregates. Finally, we confirmed the existence of similar vascular and BBB changes in HD patients.

Interpretation: Taken together, our results provide evidence for alterations in the cerebral vasculature in HD leading to BBB leakage, both in the R6/2 mouse model and in HD patients, a phenomenon that may in turn have potential pathophysiological implications.

Key words: Cerebral vasculature, blood-brain barrier, mutant huntingtin, R6/2, tight junctions, vesicles

INTRODUCTION

Huntington's disease (HD) is an autosomal dominant neurodegenerative disorder that presents with a range of motor, cognitive, psychiatric and metabolic abnormalities. The clinical and pathological signs of the disease result from an abnormal CAG repeat expansion in exon 1 of the *huntingtin* gene, leading to the expression of the mutant huntingtin (mHtt) protein. This mutated huntingtin isoform encodes a polyglutamine stretch that gives rise to oligomers and fibrillary structures [1]. While the pathogenic effects of aggregate formation are still being debated [3-6], the available evidence suggests that the oligomeric form of the protein is the most toxic (for review, see [7]).

Given the genetic origin of HD, the process of mHtt oligomerization, aggregate formation and associated pathology has been believed to be essentially cell-autonomous. However, a number of recent studies have challenged this assumption [8,9]. In particular, our recent post-mortem analysis of HD patients who had been in receipt of fetal striatal allografts has revealed the presence of mHtt aggregates within the genetically-unrelated grafted tissue [10]. These mHtt aggregates were found almost exclusively within the extracellular matrix of the grafted tissue, and in cells associated with blood vessels as well as within perivascular macrophages [10]. This not only provided the first *in vivo* demonstration of mHtt spread in patients with a monogenic human neurodegenerative disorder of the central nervous system (CNS), but also suggested the existence of non cell-autonomous mechanisms of pathological protein transmission. These findings, along with recent work demonstrating that mHtt is expressed in peripherally circulating monocytes [11], raise the intriguing possibility that mHtt might be transported into the CNS via peripheral blood-borne cells. Despite the fact that the latter cells have limited access to the CNS due to the blood-brain-barrier (BBB), there is increasing evidence that a number of neurodegenerative disorders are associated with alterations in the cerebrovasculature, including the neurovascular unit and the BBB [12,13], which may facilitate the access of peripheral cells to the CNS compartment.

In this regard, we and others have recently reported that there are changes in cerebrovascular vessel density in HD patients and in transgenic mouse models of the disease [14,15]. However, aside from a few studies conducted in the 1990s showing reduced cerebral blood flow in the caudate

of HD patients secondary to cell loss [16-19], the vascular changes and integrity of the BBB have not been systematically investigated despite their obvious clinical and therapeutic relevance. We now present the first extensive study in both the R6/2 transgenic mouse model and patients with HD investigating mHtt expression in cells associated with blood vessels, as well as its impact on vascular changes and BBB permeability.

MATERIALS AND METHODS

Human studies

Participants

HD patients and age- and sex-matched control subjects were recruited from the HD clinic at the John van Geest Centre for Brain Repair (Cambridge, UK) (**Table 1**). None of the subjects had a history of vascular disease. Participants provided informed consent, and procedures were conducted under the Research Ethics Committee approval (REC 12/EE/0528). Burden of disease score was calculated as described [20].

3T MRI

Subjects were scanned using a 3T Siemens TimTrio system. Structural imaging was achieved with an MPRAGE acquisition (TR/TI/TE: 2300/900/3 ms; FOV: 25.6×24.0×17.6mm^3; matrix 256×240×176). DCE imaging based on a 3D-FLASH sequence used TR/TE, 3.5/1.4ms; FOV 230×230×85 mm^3; matrix 128×128×17; 25% zero-filling and two-fold acceleration for 6s temporal resolution. To measure T_1, images (flip angles (FA) from 5 to 35°) were acquired. The dynamic series consisted of 120 frames (FA 25°) acquired over 12 minutes, gadobutrol (9 ml; 1.0 mmol/ml Gd-DTPA; Bayer) was injected into the medial cubital vein at 5 ml/s followed by a saline flush of 20 ml. Structural images were corrected for inhomogeneity, registered to a template (Montreal Neurological Institute) and segmented into gray matter, white matter and cerebrospinal fluid portions using Statistical Parametric Mapping 12 (SPM12) (Wellcome Trust Centre for Neuroimaging). The Parker arterial input function [21] was used to fit permeability (K_{trans}) and voxelwise vessel fraction using Patlak analysis [22]. Statistical parametric mapping (SPM) was used

to produce voxelwise statistical parametric maps for K_{trans} group differences between patients and controls, masked using segmented grey and white matter maps. Type I errors due to multiple comparisons were controlled using family-wise error correction.. Hand-drawn regions of interests (ROIs) for the caudate and putamen were used to extract mean values. ROIs were produced using Analyze 12 (Mayo Clinic) and calculated permeability maps were transformed to match the higher-resolution structural MRI space using SPM12. Within each ROI, outlying values were excluded by taking the mean of values within the 1-99% percentiles.

7T MRI

Subjects were scanned on a 7T Philips Achieva system with head transmit and 32-channel receive coil, using image-based shimming to correct for field inhomogeneities. A Look-Locker echo-planar imaging (LL-EPI), flow-sensitive alternating inversion recovery (FAIR) arterial spin labeling (ASL) protocol[23-25] was used to generate arterial cerebral blood volume (aCBV) maps. Acquisition parameters: 21 LL-EPI readout pulses per 4.8 s label/control pair; GE-EPI readout (FA 55^{o}; TE 10 ms; FOV 216 mm x 192 mm and 2 mm in-plane resolution; slice thickness 4 mm); in-plane saturation; initial delay 150 ms, LL-EPI readout spacing 100 ms; 15/230 mm selective/non-selective inversion; 20 averages. For coverage of caudate/putamen/cortical gray matter, aCBV acquisitions were collected at 3 slice locations parallel to the AC-PC line (centered on the caudate and putamen, and 10 and 20 mm above). A base magnetization image was collected to estimate M_{0blood} for aCBV quantification, and inversion-recovery images to form a T_1 map. A 0.8 mm isotropic phase-sensitive inversion recovery (PSIR) anatomical image was acquired to define ROIs and assess atrophy. A Turbo Field EPI was used to generate magnetic resonance angiograms (MRA) (EPI factor 3; TR/TE 19.12/10.34 ms; FA 7°; voxel size 0.6 mm isotropic; matrix 384 x 384 x 100). Caudate and putamen ROIs were defined from the PSIR scan, and a cortical gray matter ROI was formed by thresholding the T_1 map at $1.7 \leq T_1 \leq 2.3$ s. Average aCBV (ml blood/100 ml tissue) and arterial transit time (s) within each ROI was calculated using a two-compartment vascular kinetic model as described in[23,25].

Post-mortem human brain tissue

Post-mortem human brain tissue was obtained from the Cambridge Brain Bank and used under local ethical approval (REC 01/177). The severity of HD was graded by a certified pathologist according to the Vonsattel grading system [26,27]. All post-mortem analyses conducted in Canada were approved by the *Comité d'éthique de la recherche du CHU de Québec* (#A13-02-1138). The CAG repeat size in the *HTT* gene was determined for each HD case by DNA sequencing (Sanger Sequencing Services; Laragen Inc.) (see **Suppl Table 1** for details on the sample used).

Immunofluorescence imaging of human tissue

Paraffin-embedded sections were stained as described {Arsenault et al., 2015, #94413}. For confocal microscopy, tissue preparation and immunofluorescent staining, procedures were performed as described [10,14]. Images were acquired using the simultaneous confocal/multichannel fluorescence mode of the TISSUEscope™ digital slide scanner (Huron Digital Pathology). Whole brain sections were digitized using magnification ≤ 40X. The confocal optical slices were merged into a reconstructed volume using software available from Huron Digital Pathology. Sections were imaged with a Fluoview FV1000 confocal microscope system equipped with 559-nm and 635-nm laser diodes and an Ar 488-nm laser (Olympus Canada Inc.). For the quantification of the percentage of vWF+ and laminin+ blood vessels expressing EM48+ aggregates, m = 627 and m = 173 were assessed in 8 and 6 fields of view, respectively. Diameter of blood vessels assessed ranged from 5 to 94 µm.

Blood vessel density, morphometric and extravasation analyses

Images of the entire putamen were taken at 2000-µm intervals using Stereo Investigator software (MBF Bioscience) integrated with an E800 Nikon microscope (Nikon Canada) using an automated platform. Analyses were performed using ImageJ (National Institutes of Health, http://imagej.nih.gov/ij). For blood vessel leakage analysis, masks from collagen IV and fibrin were obtained and assigned to a color (magenta for blood vessels and yellow for albumin). After merging images, magenta and white (from the colocalization of magenta and yellow) were removed, leaving only the fibrin staining (yellow) (cf. **Fig. 6B**).

Western blot analysis and multiplex angiogenesis ELISA assay of human tissues

Approximately 100 mg of frozen samples of putamen from HD patients andmatched healthy controls (**Suppl. Table 1**) were processed to extract proteins for western blotting according to previously published protocols {Drouin-Ouellet et al., 2014, #31993}. For the multiplex assay, samples were simultaneously analyzed for 9 human markers associated with angiogenesis and BBB permeability, using a Q-Plex™ Human Angiogenesis assay (Quansys Bioscience), according to the manufacturer's instructions.

Animal study

Animals

R6/2 mice [31] were purchased from Jackson Laboratory (Bar Harbor) and bred in the John van Geest Centre for Brain Repair animal facility (Cambridge, UK). Tissue from ear biopsies was sent to Laragen Inc. for genotyping. All mice were housed in a temperature-controlled (22°C) room under standard diurnal conditions (12-h light/dark cycle). Food and water were provided *ad libitum*. Animal handling, testing, and other procedures were carried out in the UK in accordance with the UK Animals (Scientific Procedures) Act 1986, and with the appropriate Home Office Personal and Project Licenses. Animal handling, testing, and other procedures carried out in Canada were in accordance with the Canadian Guide for the Care and Use of Laboratory Animals and were approved by the Institutional Policy of the Centre de recherche du CHU de Québec (CHUQ). For all experiments, 11-15 weeks old R6/2 were used.

In situ cerebral perfusion

In situ cerebral perfusion was performed using established protocols [32,33]. To measure the volume and the surface of the vascular network, each mouse was perfused for 240 s with [^{14}C]sucrose (0.6 µCi/ml of perfusion buffer; 412 mCi·mmol^{-1}; Moravek Biochemicals), a vascular space marker that does not cross the BBB, and [^{3}H]diazepam (0.3 µCi/ml of perfusion buffer; 83.7 Ci·mmol^{-1}; Perkin Elmer), a highly lipophilic drug that readily crosses the BBB in a flow-limited fashion. The right striatum was dissected and the left hemisphere was post-fixed for 48 h in 4% PFA, and cryoprotected in 20% (w/v) sucrose for the analysis of blood vessel density and morphometrics. The calculations of vascular volumes were performed as described previously [33,34].

Mouse tissue preparation and immunofluorescence

Mouse brains were collected, sliced and free-floating sections were stained as previously described {Drouin-Ouellet et al., 2014, #31993} (See **Table 2** for antibody list). For the lectin/albumin double labeling, DyLight 594-conjugated lectin (Vector Laboratories, 1:100) was used. Sections were observed as described above (cf. *Immunofluorescence imaging of human tissue*)

Blood vessel density, morphometric and extravasation analyses

Three striatal sections per mice, 250 µm apart, were selected, and a 20X magnification image was taken in each quadrant of the striatum. Extravasation analysis of albumin was performed as described for fibrin in the human study. Analyses were performed using ImageJ.

Brain perfusion and vascular casting for scanning electron microscopy

Mice were perfused first with 0.9% saline, followed by 100% ethanol. LR White Accelerator wasadded to LR White Embedding Medium (Electron Microscopy Science), and mice were immediately perfused using this mixture. Tissue was incubated overnight at 37°C and the striatum was dissected and soaked in a 4 M KOH solution for 4 weeks. Cast samples were then mounted onto a metallic support and observed with a scanning electron microscope JEOL 6360LV set at 30 kV.

Transmission electron microscopy tissue preparation and analyses

Mice were subjected to intracardiac perfusion under deep anesthesia first with 0.1 M sodium cacodylate, and then with 2.5% glutaraldehyde and 2% PFA and tissue was prepared as described (REF Richard; Jeremy?). Observations were performed using a Tecnai G2 Spirit Biotwin electron microscope (FEI) set at a 80-kV acceleration voltage. Mesures of tight junction (TJ) were performed on 39 to 47 TJs per animal. The portion of the endothelium circumference covered by pericytes was measured on 18 to 20 blood vessels per animal. Density of various types of vesicles were quantified according to previously published descriptions [36] on 20 vessels per animal. Blood vessel subtypes (capillaries or venules) were assigned as described (REF). All analyses were

performed using the ImageJ software.

Immunoelectron microscopy

Mice were perfused with 4% PFA in 0.1 M sodium cacodylate and brains were fixed in the same solution before being prepared for immunogold labeling, which was done as described (REF) using the EM48 primary antibody and labeled with 10 nm colloidal gold-conjugated anti-mouse antibody (BBInternational, 1:100).

Real-time quantitative PCR analysis of mouse tissue

RNA was extracted from striatal tissue using RNeasy Lipid Tissue Mini Kit (Qiagen). The following primer sequences were used: PDGFβ forward, TGACCCCTCGGCCTGTGACT; PDGFβ reverse, 5'-CCGGCGGATTCTCACCGTCC-3' and the house-keeping gene GAPDH forward, 5'-GTATGTCGTGGAGTCTACTG-3', GAPDH reverse, 5'-GAGTTGTCATATTTCTCGTGGT-3'. The qPCR was performed using Brilliant III SYBR® Green QPCR Master Mix (Agilent Technologies, Inc) and a Mx3005P qPCR system (Stratagene). Relative gene level differences between groups were evaluated with the $\Delta\Delta C_t$ method.

Western blot analysis for mouse tissue

Striatal tissue (20 mg) was homogenized and Western blot experiments were carried out and quantified as described for human tissues.

Statistical analysis

For studies involving human tissue samples, the pathological grade was taken into account in all initial statistical analyses but given that no significant effect was detected, data from HD cases were pooled and compared to control subjects. Statistical significance was set at $p<0.05$. All statistical analyses were performed using Prism 6.0, SPSS Statistics version 22 and SAS (version 9.2, SAS). The *Service de Consultation Statistique* of Université Laval was consulted for some statistical analyses regarding the MRI studies.

RESULTS

Expression of mHtt pathology in cerebral blood vessels

Building on our previous observation that mHtt aggregates were found in the basal membrane of cerebral blood vessels of HD patients [10], we first assessed the expression of mHtt aggregates in all compartments of the neurovascular unit. mHtt aggregates were observed inside the basal membrane sheaths as well as in the nuclei of cells embedded in the basal membrane in both small- (5-10 µm) and large-calibre (>20 µm) blood vessels (**Fig. 1A to C**). mHtt aggregates were found to colocalize with vWF-labelled endothelial cells (**Fig. 1D to G**), as well as α-SMA+ cells within the basal membrane (**Fig. 1H**) and CD163+ perivascular macrophages (**Fig. 1I**). EM48+ aggregates were found in the basal membrane and endothelium of 3 and 7% of cortical blood vessels, respectively. Similar to our observations in post-mortem samples from HD cases, EM48+ aggregates could also be found both in the basal membrane and inside cells that were embedded in the basal membrane of small and larger blood vessels in R6/2 mice, specifically within α-SMA+ pericytes or smooth muscle cells (**Fig. 2A to D**), as well as within CD31+ endothelial cells (**Fig. 2E**).

Vascular changes in the putamen of HD patients

Given that mHtt can impair mitochondrial integrity and elicit oxidative stress, which may affect the physiology of cells composing the cerebral vasculature [37,38], we next investigated morphological, structural and functional changes in blood vessels in the context of HD using MRI and post-mortem HD tissue. There was a significant increase in aCBV in cortical gray matter in the HD cohort ($p < 0.05$; **Fig. 3A**), but not in the putamen nor caudate, and the aCBV did not correlate with gray matter volume (data not shown). No significant difference was found in arterial transit time between HD and control participants (**Fig. 3B, C**). Qualitative assessment of 7T MRA of patients did not yield overt differences in blood vessel density for large-calibre blood vessels (> 600 µm), although it was not possible to perform proper quantifications given the limited number of collected angiograms (**Fig. 3D**). We thus used post-mortem tissue samples to specifically assess potential morphological differences in blood vessels of the putamen of HD patients. Measurements of cerebral blood vessel density revealed an increase in HD subjects ($p < 0.001$; **Fig. 4A, B**), independent of putaminal atrophy ($R^2 = 0.11$; $p = 0.15$; **Fig. 4C**). We found no difference

in the diameter of small- or medium-sized blood vessels (5-10 µm and 10-20 µm diameter, respectively) between HD and matched controls (**Fig. 4D**), nor in the Feret diameter (data not shown). However, we found an increased proportion of small blood vessels (5-10 µm) as compared to medium-sized blood vessels (10-20 µm) in the putamen of HD patients ($p < 0.01$; **Fig. 4E**). Interestingly, a significant positive correlation was found between the size of blood vessels and the surface area of the putamen ($R^2 = 0.37$; $p < 0.01$; **Fig. 4F**) as well as between the Feret diameter and the surface area of the putamen ($R^2 = 0.26$; $p < 0.05$; **Fig. 4G**), suggesting that putaminal atrophy was accompanied by a reduction in blood vessel size. Finally, we measured the wall thickness of the basal membrane, given that this is among the characteristic features of vascular pathology in other neurodegenerative diseases such as Alzheimer, but did not detect any differences (**Fig. 4H**). Overall, although the morphology of large-calibre blood vessels remains intact in the brain of HD patients, there is an increase in the number of small blood vessels, an effect that appears to occur concurrently with putaminal degeneration.

Morphological changes in striatal blood vessels of R6/2 mice

Given the similar pattern of expression of mHtt aggregates within the neurovascular units of the R6/2 mouse and HD patients, we further used the R6/2 mouse to investigate blood vessel changes. In line with our observations in human post-mortem samples, the density of striatal blood vessels in R6/2 mice was increased ($p < 0.01$; **Fig. 5A, B**). This was accompanied by a reduction in the average Feret diameter of blood vessels ($p < 0.05$; **Fig. 5C**), although apparent differences in size vanished upon distinguishing arterioles from capillaries and venules (**Fig. 5D**), suggesting that the decrease in Feret diameter of blood vessels in R6/2 mice is not specific to particular blood vessel subtype(s). Scanning electron microscopy revealed further abnormalities in the striatal vascular network. Indeed, the vascular network of R6/2 mice was characterized by a smaller ratio of the diameter of branches to that of the parent vessel, compared to WT littermates ($p < 0.05$; **Fig. 5E, F**). Furthermore, several aborted branch buds were observed in the striatum of the R6/2, but not of WT littermates (**Fig. 5E**). We next assessed whether these structural changes had an impact on the volume of the striatal vascular network, using *in situ* cerebral perfusion, and found that the V_{vasc} of the striatal network in R6/2 mice and WT

littermates was similar. In agreement with this, brain uptake clearance (Cl_{up}) of [^{3}H]diazepam, which measures the surface area of the vascular network, was also similar in R6/2 mice and controls (**Fig. 5G**). This data thus supports the scanning electron microscopy and immunofluorescence data, showing that the brain vasculature anomalies were restricted to smaller vessels.

BBB leakage in HD patients

We next assessed whether the observed morphological and structural changes in cerebral blood vessels of HD patients are associated with functional impairments of the BBB. Decreases in expression of proteins forming the TJs of the BBB, such as claudin-5 and occluding, have been associated with increased permeability [39]. Western blot analysis revealed a significant decrease in both proteins ($p < 0.01$ and $p < 0.05$, respectively) in the putamen of HD patients (**Fig. 6A**). While we did not detect a significant change in VEGF expression, a significant increase in other markers associated with increased BBB permeability such as PDGFβ ($p < 0.05$), HGF ($p < 0.001$), IL-8 ($p < 0.05$), TIMP1 ($p < 0.05$) and TIMP2 ($p < 0.05$; **Fig. 6D**) was observed. To confirm that BBB breakdown occurred in the putamen of HD patients, we next measured the levels of extravascular fibrin deposition [29,40] and found it to be increased 2.5-fold when compared to controls ($p < 0.05$; **Fig. 6B, C**). Finally, we assessed whether BBB leakage might be detected in mild-to-moderate stage HD patients using a dynamic contrast-enhanced MRI method. Overall, we found a trend towards an increased leakage in the caudate and putamen of HD patients as compared to age- and sex-matched control subjects (**Fig. 7A, B**). Interestingly, BBB leakage in the right caudate significantly correlated with the burden of disease score ($R^2 = 0.69$; $p < 0.05$; **Fig. 7C**), suggesting that BBB permeability increases with disease progression in HD.

Paracellular and transcytotic alterations in the striatum of R6/2 mice

We further characterized paracellular transport and transcytosis across the BBB in R6/2 mice. While TJ length in the striatum of R6/2 mice and WT mice was similar, the extracellular cleft on the side of the lumen was wider in the transgenic animals ($p < 0.05$, **Fig. 8A**). Additionally, TJs had a wider angle with respect to the lumen in R6/2 mice ($p < 0.05$, **Fig. 8B, C**), suggesting a random

junctional alignment in the HD model [41]. Moreover, claudin-5 and occludin were both significantly decreased in R6/2 mice ($p < 0.05$; **Fig. 8D**). Finally, given that TJs may facilitate leukocyte diapedesis through weakened inter-endothelial contact points [42], we looked for the presence of perivascular cells and found an increased number of CD45+ leukocytes attached to the blood vessel walls in R6/2 (**Fig. 8E**).

In addition to the paracellular barrier formed by the TJs, the BBB provides a transcellular hindrance [43]. We thus assessed transcytosis in R6/2 mice and found an increase in the total number of vesicles in the endothelium of striatal blood vessels ($p < 0.05$; **Fig. 9A**) [36]. Upon assessing the different subtypes of vesicles, we found a 5-fold increase in luminal type II vesicles - connected vesicles pinching from the luminal plasma membrane - suggesting an increase in pinocytotic events ($p < 0.05$; **Fig. 9B, C**). Immunogold labeling of EM48 also revealed the presence of gold particles in the endothelium of R6/2 mice, which were further detected within all the different subtypes of vesicles (**Fig. 9D**). In accordance with increased transcytosis in the striatum of R6/2 mice, we found a nearly 20-fold increase in extravascular albumin in transgenic mice ($p < 0.05$; **Fig. 9E**), suggesting a disruption of BBB integrity [44]. Because pericytes play an important role in BBB integrity and since pericyte-deficient mice (pdgfrb-/- mice) display increased transcytosis [41], we further assessed pericyte coverage, but did not find significant differences (**Fig. 9F**). However, mRNA expression of PDGFβ was significantly decreased ($p < 0.01$; **Fig. 9G**). Taken together, these findings suggest an increased BBB permeability in R6/2 mice, which includes increased transcytosis and paracellullar transport.

DISCUSSION

Our data provide clear evidence for ultrastructural, morphological and functional changes in cerebral blood vessels with alterations of the BBB in HD, as evidenced both in an animal model of disease, the R6/2 mouse, and in humans as shown by MRI in mild-to-moderate stage HD patients as well as in post-mortem tissue.

In this study, among different blood vessel compartments, we specifically detected the expression of mHtt aggregates in endothelial cells, in cells enclosed in the basal membrane, as well as in perivascular macrophages [10] (**Fig. 10**). Ideally, it would be informative to ascertain whether the more toxic oligomers are preferentially associated with the latter sites of mHtt aggregate accumulation, but given that no antibodies recognizing mHtt oligomers are currently available, we were unable to verify this. Nevertheless, the presence of aggregates suggests that such toxic species of mHtt are likely to be present in these compartments.

While the specific pathophysiological effects of mHtt expression within these neurovascular compartments are yet unknown, neural activity has been shown to affect vascular structure [45-47]. Therefore, it is possible that the changes reported here are secondary to the effects of mHtt on neural activity, although this seems unlikely given the extent of changes observed [48-50]. In addition, brain endothelial cells contain large numbers of mitochondria as compared to peripheral endothelium, and are thus more susceptible to oxidative stress [37,38], which has been proposed as an effector of BBB damage and endothelial dysfunction through alterations in the expression of TJ-associated proteins [51]. An intrinsic dysfunction of endothelial cells secondary to their accumulation of mHtt is thus more likely to be the main determinant of the morphological and functional changes observed in our study. We have recently shown that allografts of normal tissue are not well vascularized in the brain of HD patients [14], which could reflect an intrinsic limitation of the cerebral blood vessels in HD in the remodeling and proper vascularization of new tissue. Moreover, mHtt is also expressed in astrocytes, and it has been reported mHtt expression in this cell type could mediate signs of neurological impairments associated with HD [8]. Given that astrocytes are an important component of the BBB, the expression of mHtt in these cells could also participate in the vascular impairments that occur in HD.

The finding that the size of blood vessels decreases concomitantly with the atrophy of the putamen is surprising but might be a consequence of the increased number of smaller blood vessels observed here, along with the decrease in the number of arteries. Oxygen diffusion is different in arterioles, venules and capillaries, with most oxygen diffusion taking place across the

capillary bed [52]. An increase in the total surface of capillary beds could help maintain proper oxygenation of the surrounding tissues despite a decrease in the number of larger blood vessels. This hypothesis may hold provided that the increase in capillary surface compensates for the reduced primary blood flow and dissolved oxygen flow rate that results from the decreased number of large vessels. Alternatively, a reduced rate of oxygen delivery across a compromised vascular network in HD might be the primary event that triggers a compensatory, secondary increase in vasculature. Furthermore, aCBV - which in essence measures the volume of blood in the arterial, non-capillary, component - was increased in the gray matter of HD patients, in line with previous observations in R6/2 mice [15,53]. However, the R6/2 mouse model is not characterized by overt neuronal death [31], which argues against a direct involvement of neuronal loss in the various changes in the vasculature, as does the fact that the increase in density and the decrease in the size of blood vessels have been previously reported to develop as early as 5 to 7 weeks of age in these mice [15]. Overall, the available evidence supports the existence of a vascular pathology in HD that is independent from the neuronal loss characteristic of the disease.

The HD-associated abnormalities in the vasculature reported here also have functional consequences in that the BBB is compromised in both R6/2 mice and HD patients, as we show here for the first time. Two previous studies using DCE-MRI in R6/2 mice with Gd-DTPA as a contrast agent had failed to show any BBB leakage [15,53]. However, the sensitivity of this method in small animals is lower and may thus not afford detection of subtle changes in BBB permeability. In contrast, our study now shows that in HD patients (using the same contrast agent), there is a trend towards an increased permeability of the BBB – i.e. a loss of BBB integrity – with a concomitant increase in the burden of disease score. The reason why only a trend could be definitively established probably relates to the small sample size (n=7) and the fact that we restricted our selection of participants to mild-to-moderate stage HD to avoid issues related to movement-dependent artefacts in the scanner secondary to their chorea. However, the significance of this trend is reinforced by our post-mortem analyses which revealed unequivocal signs of BBB leakage both in R6/2 mice and HD patients, including wider TJ intercellular clefts, decreased expression of BBB TJ proteins, increases in perivascular leukocytes, as well as leakage

of albumin and fibrin into the brain parenchyma [54-57].

We specifically examined the expression of claudin-5 and occludin, as they are the two major proteins associated with BBB TJs. Claudin-5 is a major functional constituent and a critical determinant of BBB paracellular permeability in mice by creating size- (< 800 Da) and charge-selective hydrophilic paracellular pores [58-60], while occludin enhances TJ tightness. Our finding of decreases in the expression of these TJ proteins in both R6/2 mice and the HD putamen, along with the increase found here in the number of leukocytes in the perivascular space of cerebral blood vessels, are likely to reflect an increase in circulating blood cells transiting into the brain of HD patients. Moreover, the extravascular accumulation of albumin in the R6/2 brain suggests an increase in transcytosis as this protein can be transported through the endothelium via transcytostic vesicles, although increased paracellular transport might also contribute to the process [61].

The extravascular accumulation of fibrin deposition that we observed in HD brains might be in accordance with this hypothesis, as it is a well-known marker of BBB leakage in human autopsy tissues [54,56,57]. The BBB is vital for protecting the CNS from systemic perturbations and from elements of the peripheral immune system, so that any impairment of its integrity could have far-reaching consequences on the health of the CNS. Thus, our data demonstrating that the integrity of the BBB is compromised and that the cerebral vasculature is considerably disrupted in HD, likely indicate that these impairments may contribute in driving the disease process. Indeed, this data provides evidence linking the well-described peripheral immune changes of HD to the CNS pathology [62,63]. In particular, the changes reported herein in both mice and human could allow peripheral blood leukocytes to enter the CNS more easily, where they might act as vehicles for mHtt transfer into the brain, or exacerbate neuronal death by participating in the cerebral inflammatory response. The detection of mHtt in transcytotic vesicles, in conjunction with the increased transcytosis observed in R6/2 mice, suggests that an exchange of mHtt between the blood and the brain is possible – which has obvious implications for HD pathogenesis (**Fig. 10**).

In summary, the clinical and pre-clinical data reported here reveals that mHtt is expressed in various cells associated with cerebral blood vessels, which is likely to contribute to the structural and functional changes that we find in the BBB. These changes may be important pathogenic players allowing a greater access of both mHtt and immune cells to the diseased CNS than previously recognized. Overall, the present study not only reveals a new pathogenic process underlying HD but also uncovers novel, potentially important therapeutic avenues.

POTENTIAL CONFLICTS OF INTEREST

The authors declare no conflict of interest.

ACKNOWLEDGMENTS

This study was funded by the Canadian Institutes of Health Research to Francesca Cicchetti who is also recipient of a National Researcher career award from the Fonds de recherche du Québec en santé (FRQS) providing salary support and operating funds. Part of this study was also funded by the Cotswold Trust to Roger Barker. Janelle Drouin-Ouellet is supported by a FRQS post-doctoral fellowship. Giulia Cisbani is supported by a scholarship from the Huntington's Disease Society of America Inc. (HDSA). Isabelle St-Amour is supported by a CIHR – Huntington Society of Canada post-doctoral fellowship. Roger Barker is supported by an NIHR award of a Biomedical Research Centre to the University of Cambridge and Addenbrooke's Hospital. Salary support for Steve Lacroix was provided by the FRQS. The Sir Peter Mansfield Magnetic Resonance Centre has grant support from the Medical Research Council (MRC) for the 7 Tesla MRI system and Richard Dury is supported by an MRC studentship. The authors would like to thank Mr. Richard Janvier for his very skilful electron microscopy preparation and analyses, the Cambridge Brain Bank for the post-mortem tissue which is supported by a grant to the NIHR Cambridge Biomedical Research Centre and Huron Digital Pathology for their collaboration on this work and for generously providing the TISSUEscope^{TM} technology. We also acknowledge the Bioimaging platform of the Infectious Disease Research Centre, funded by an equipment and infrastructure grant from the Canadian Foundation for Innovation (CFI). We would also like to thank Dr. Aviva Tolkovsky for her helpful comments on this manuscript and Dr. Richard Poulin for his valuable editing services.

AUTHORSHIP

JDO participated to the design of the experiments, performed part of the animal studies and the human post-mortem studies, analyzed and interpreted most data and wrote the manuscript.
SJS designed, conducted and analyzed the 3T MRI experiment and participated in the interpretation of the 7T MRI data.
GC performed some of the immunofluorescent stainings and did the confocal image acquisition, as well as some of the WB experiments.
ML was involved in the design of the transmission electron microscopy experiments and performed related analyses.
WLK participated to the design of some experiments and performed part of the animal study.
MSP performed some of the immunofluorescent stainings as well as some of the image acquisition and WB experiments.
RJD acquired and analyzed the 7T MRI data.
ISA performed and analyzed the qPCR experiments.
WA performed and analyzed the *in situ* cerebral perfusion experiments.
SLM recruited patients and coordinated the MRI studies.
FCa designed and interpreted data related to the *in situ* cerebral perfusion experiments.
SL provided expertise for some immunofluorescent stainings and revised the manuscript.
PAG participated in the design and interpretation of the 7T MRI experiments.
STF participated in the design, analyses and interpretation of the 7T MRI experiments.
RAB recruited the patients, provided the post-mortem brain tissue, the R6/2 mice and revised the manuscript.
FCi initiated the study and was involved in the experimental design and data interpretation. She supervised the project and was involved in writing parts of the manuscript.

References

1. Scherzinger, E, Lurz, R, Turmaine, M et al. Huntingtin-encoded polyglutamine expansions form amyloid-like protein aggregates in vitro and in vivo. Cell 1997;90:549-558.
2. Huang, CC, Faber, PW, Persichetti, F et al. Amyloid formation by mutant huntingtin: threshold, progressivity and recruitment of normal polyglutamine proteins. Somat Cell Mol Genet 1998;24:217-233.
3. Arrasate, M, Mitra, S, Schweitzer, ES et al. Inclusion body formation reduces levels of mutant huntingtin and the risk of neuronal death. Nature 2004;431:805-810.
4. Muchowski, PJ. Protein misfolding, amyloid formation, and neurodegeneration: a critical role for molecular chaperones? Neuron 2002;35:9-12.
5. Taylor, JP, Tanaka, F, Robitschek, J et al. Aggresomes protect cells by enhancing the degradation of toxic polyglutamine-containing protein. Hum Mol Genet 2003;12:749-757.
6. Webb, JL, Ravikumar, B, Rubinsztein, DC. Microtubule disruption inhibits autophagosome-lysosome fusion: implications for studying the roles of aggresomes in polyglutamine diseases. Int J Biochem Cell Biol 2004;36:2541-2550.
7. Cisbani, G, Cicchetti, F. An in vitro perspective on the molecular mechanisms underlying mutant huntingtin protein toxicity. Cell Death Dis 2012;3:e382.
8. Bradford, J, Shin, JY, Roberts, M et al. Expression of mutant huntingtin in mouse brain astrocytes causes age-dependent neurological symptoms. Proc Natl Acad Sci U S A 2009;106:22480-22485.
9. Lee, CY, Cantle, JP, Yang, XW. Genetic manipulations of mutant huntingtin in mice: new insights into Huntington's disease pathogenesis. FEBS J 2013;280:4382-4394.
10. Cicchetti, F, Lacroix, S, Cisbani, G et al. Mutant huntingtin is present in neuronal grafts in Huntington disease patients. Ann Neurol 2014;76:31-42.
11. Weiss, A, Trager, U, Wild, EJ et al. Mutant huntingtin fragmentation in immune cells tracks Huntington's disease progression. J Clin Invest 2012;122:3731-3736.
12. Kook, SY, Hong, HS, Moon, M et al. Abeta(1)(-)(4)(2)-RAGE interaction disrupts tight junctions of the blood-brain barrier via Ca(2)(+)-calcineurin signaling. J Neurosci 2012;32:8845-8854.
13. Zlokovic, BV. Neurovascular pathways to neurodegeneration in Alzheimer's disease and other disorders. Nat Rev Neurosci 2011;12:723-738.
14. Cisbani, G, Freeman, TB, Soulet, D et al. Striatal allografts in patients with Huntington's disease: impact of diminished astrocytes and vascularization on graft viability. Brain 2013;136:433-443.
15. Lin, CY, Hsu, YH, Lin, MH et al. Neurovascular abnormalities in humans and mice with Huntington's disease. Exp Neurol 2013;250:20-30.
16. Harris, GJ, Aylward, EH, Peyser, CE et al. Single photon emission computed tomographic blood flow and magnetic resonance volume imaging of basal ganglia in Huntington's disease. Arch Neurol 1996;53:316-324.
17. Harris, GJ, Codori, AM, Lewis, RF et al. Reduced basal ganglia blood flow and volume in pre-symptomatic, gene-tested persons at-risk for Huntington's disease. Brain 1999;122:1667-1678.
18. Hasselbalch, SG, Oberg, G, Sorensen, SA et al. Reduced regional cerebral blood flow in Huntington's disease studied by SPECT. J Neurol Neurosurg Psychiatry 1992;55:1018-1023.
19. Hayden, MR, Hewitt, J, Stoessl, AJ et al. The combined use of positron emission tomography and DNA polymorphisms for preclinical detection of Huntington's disease. Neurology 1987;37:1441-1447.
20. Penney, JBJ, Vonsattel, JP, MacDonald, ME et al. CAG repeat number governs the development rate of pathology in Huntington's disease. Ann Neurol 1997;41:689-692.
21. Parker, GJ, Roberts, C, Macdonald, A et al. Experimentally-derived functional form for a

population-averaged high-temporal-resolution arterial input function for dynamic contrast-enhanced MRI. Magn Reson Med 2006;56:993-1000.
22. Patlak, CS, Blasberg, RG, Fenstermacher, JD. Graphical evaluation of blood-to-brain transfer constants from multiple-time uptake data. J Cereb Blood Flow Metab 1983;3:1-7.
23. Brookes, MJ, Morris, PG, Gowland, PA, Francis, ST. Noninvasive measurement of arterial cerebral blood volume using Look-Locker EPI and arterial spin labeling. Magn Reson Med 2007;58:41-54.
24. Croal, PL, Hall, EL, Driver, ID et al. The effect of isocapnic hyperoxia on neurophysiology as measured with MRI and MEG. Neuroimage 2014
25. Francis, ST, Bowtell, R, Gowland, PA. Modeling and optimization of Look-Locker spin labeling for measuring perfusion and transit time changes in activation studies taking into account arterial blood volume. Magn Reson Med 2008;59:316-325.
26. Vonsattel, JP, Myers, RH, Stevens, TJ et al. Neuropathological classification of Huntington's disease. J Neuropathol Exp Neurol 1985;44:559-577.
27. Vonsattel, JP, DiFiglia, M. Huntington disease. J Neuropathol Exp Neurol 1998;57:369-384.
28. Kirk, J, Plumb, J, Mirakhur, M, McQuaid, S. Tight junctional abnormality in multiple sclerosis white matter affects all calibres of vessel and is associated with blood-brain barrier leakage and active demyelination. J Pathol 2003;201:319-327.
29. Sengillo, JD, Winkler, EA, Walker, CT et al. Deficiency in mural vascular cells coincides with blood-brain barrier disruption in Alzheimer's disease. Brain Pathol 2013;23:303-310.
30. Smith, PK, Krohn, RI, Hermanson, GT et al. Measurement of protein using bicinchoninic acid. Anal Biochem 1985;150:76-85.
31. Mangiarini, L, Sathasivam, K, Seller, M et al. Exon 1 of the HD gene with an expanded CAG repeat is sufficient to cause a progressive neurological phenotype in transgenic mice. Cell 1996;87:493-506.
32. Alata, W, Paris-Robidas, S, Emond, V et al. Brain uptake of a fluorescent vector targeting the transferrin receptor: a novel application of in situ brain perfusion. Mol Pharm 2014;11:243-253.
33. Ouellet, M, Emond, V, Chen, CT et al. Diffusion of docosahexaenoic and eicosapentaenoic acids through the blood-brain barrier: An in situ cerebral perfusion study. Neurochem Int 2009;55:476-482.
34. Dagenais, C, Rousselle, C, Pollack, GM, Scherrmann, JM. Development of an in situ mouse brain perfusion model and its application to mdr1a P-glycoprotein-deficient mice. J Cereb Blood Flow Metab 2000;20:381-386.
35. Franklin, KBJ, Paxinos, G. The mouse brain in stereotaxic coordinates. New York: Academic Press, 2008.
36. Ben-Zvi, A, Lacoste, B, Kur, E et al. Mfsd2a is critical for the formation and function of the blood-brain barrier. Nature 2014;509:507-511.
37. Rizzo, MT, Leaver, HA. Brain endothelial cell death: modes, signaling pathways, and relevance to neural development, homeostasis, and disease. Mol Neurobiol 2010;42:52-63.
38. Xu, J, Chen, S, Ku, G et al. Amyloid beta peptide-induced cerebral endothelial cell death involves mitochondrial dysfunction and caspase activation. J Cereb Blood Flow Metab 2001;21:702-710.
39. Jiao, H, Wang, Z, Liu, Y et al. Specific role of tight junction proteins claudin-5, occludin, and ZO-1 of the blood-brain barrier in a focal cerebral ischemic insult. J Mol Neurosci 2011;44:130-139.
40. Tomimoto, H, Akiguchi, I, Suenaga, T et al. Alterations of the blood-brain barrier and glial cells in white-matter lesions in cerebrovascular and Alzheimer's disease patients. Stroke 1996;27:2069-2074.
41. Daneman, R, Zhou, L, Kebede, AA, Barres, BA. Pericytes are required for blood-brain barrier integrity during embryogenesis. Nature 2010;468:562-566.
42. Garrido-Urbani, S, Bradfield, PF, Lee, BP, Imhof, BA. Vascular and epithelial junctions: a barrier for leucocyte migration. Biochem Soc Trans 2008;36:203-211.

43. Siegenthaler, JA, Sohet, F, Daneman, R. 'Sealing off the CNS': cellular and molecular regulation of blood-brain barriergenesis. Curr Opin Neurobiol 2013;23:1057-1064.
44. Tibbling, G, Link, H, Ohman, S. Principles of albumin and IgG analyses in neurological disorders. I. Establishment of reference values. Scand J Clin Lab Invest 1977;37:385-390.
45. Black, JE, Sirevaag, AM, Greenough, WT. Complex experience promotes capillary formation in young rat visual cortex. Neurosci Lett 1987;83:351-355.
46. Black, JE, Isaacs, KR, Anderson, BJ et al. Learning causes synaptogenesis, whereas motor activity causes angiogenesis, in cerebellar cortex of adult rats. Proc Natl Acad Sci U S A 1990;87:5568-5572.
47. Lacoste, B, Comin, CH, Ben-Zvi, A et al. Sensory-related neural activity regulates the structure of vascular networks in the cerebral cortex. Neuron 2014;83:1117-1130.
48. Hodgson, JG, Agopyan, N, Gutekunst, CA et al. A YAC mouse model for Huntington's disease with full-length mutant huntingtin, cytoplasmic toxicity, and selective striatal neurodegeneration. Neuron 1999;23:181-192.
49. Panov, AV, Gutekunst, CA, Leavitt, BR et al. Early mitochondrial calcium defects in Huntington's disease are a direct effect of polyglutamines. Nat Neurosci 2002;5:731-736.
50. Zeron, MM, Hansson, O, Chen, N et al. Increased sensitivity to N-methyl-D-aspartate receptor-mediated excitotoxicity in a mouse model of Huntington's disease. Neuron 2002;33:849-860.
51. Carrano, A, Hoozemans, JJ, van der Vies, SM et al. Amyloid Beta induces oxidative stress-mediated blood-brain barrier changes in capillary amyloid angiopathy. Antioxid Redox Signal 2011;15:1167-1178.
52. Intaglietta, M, Johnson, PC, Winslow, RM. Microvascular and tissue oxygen distribution. Cardiovasc Res 1996;32:632-643.
53. Cepeda-Prado, E, Popp, S, Khan, U et al. R6/2 Huntington's disease mice develop early and progressive abnormal brain metabolism and seizures. J Neurosci 2012;32:6456-6467.
54. Akiguchi, I, Tomimoto, H, Suenaga, T et al. Blood-brain barrier dysfunction in Binswanger's disease; an immunohistochemical study. Acta Neuropathol 1998;95:78-84.
55. Aube, B, Levesque, SA, Pare, A et al. Neutrophils mediate blood-spinal cord barrier disruption in demyelinating neuroinflammatory diseases. J Immunol 2014;193:2438-2454.
56. Dallasta, LM, Pisarov, LA, Esplen, JE et al. Blood-brain barrier tight junction disruption in human immunodeficiency virus-1 encephalitis. Am J Pathol 1999;155:1915-1927.
57. Kwon, EE, Prineas, JW. Blood-brain barrier abnormalities in longstanding multiple sclerosis lesions. An immunohistochemical study. J Neuropathol Exp Neurol 1994;53:625-636.
58. Anderson, JM, Van Itallie, CM. Physiology and function of the tight junction. Cold Spring Harb Perspect Biol 2009;1:a002584.
59. Morita, K, Sasaki, H, Furuse, M, Tsukita, S. Endothelial claudin: claudin-5/TMVCF constitutes tight junction strands in endothelial cells. J Cell Biol 1999;147:185-194.
60. Nitta, T, Hata, M, Gotoh, S et al. Size-selective loosening of the blood-brain barrier in claudin-5-deficient mice. J Cell Biol 2003;161:653-660.
61. Quagliarello, VJ, Ma, A, Stukenbrok, H, Palade, GE. Ultrastructural localization of albumin transport across the cerebral microvasculature during experimental meningitis in the rat. J Exp Med 1991;174:657-672.
62. Bouchard, J, Truong, J, Bouchard, K et al. Cannabinoid receptor 2 signaling in peripheral immune cells modulates disease onset and severity in mouse models of Huntington's disease. J Neurosci 2012;32:18259-18268.
63. Kwan, W, Magnusson, A, Chou, A et al. Bone marrow transplantation confers modest benefits in mouse models of Huntington's disease. J Neurosci 2012;32:133-142.

FIGURE LEGENDS

Table 1. Demographic details of the participants involved in the MRI studies. Abbreviations: MRI: magnetic resonance imaging; nk: not known; T: Tesla; TFC: total functional capacity; UHDRS: Unified Huntington's disease rating scale.

Table 2. List of the primary antibodies used in the study. Abbreviations: IF: immunofluorescence; IG: immunogold; WB: western blot.

Suppl Table 1. Demographic details of the post-mortem brain sample cases. Abbreviations: CTL: controls; HD: Huntington's Disease; nk: not known; PM: post-mortem; SD: standard deviation.

Figure 1. Localization of mHtt aggregates within the blood vessels of HD patients. (**A to C**) EM48+ mHtt aggregates (*green*) were found within the laminin+ basal membrane (*red*) and in the nuclei of cells lodged within the basal membrane, both in large-calibre (**A, A', B, B'**) and small blood vessels (**C, C'**). (**D-G**) EM48+ mHtt aggregates (*green*) were found inside the neurovascular unit, in vWF+ endothelial cells (*red* in **D** to **G**), αSMA+ vascular smooth muscle cells (*red* in **H**) and in CD163+ perivascular macrophages (*gray* in **H**). Abbreviations: α-SMA: alpha-smooth muscle actin; DAPI: 4', 6-diamidino-2-phenylindole; vWF: von Willbrand factor. Scale bars **A, B, C** = 50 µm; **A', B'** = 10 µm; **C'** = 20 µm; **D, E, F** = 10 µm; **G, H, I** = 15 µm.

Figure 2. Localization of mHtt aggregates within blood vessels of R6/2 mice. (**A to D**) EM48+ mHtt aggregates (*green*) were found within the laminin+ basal membrane (**A, B**: *gray*; **C, D**: *blue*) and cells embedded in it, including αSMA+ cells (*red*). More specifically, mHtt aggregates were found within the nucleus (DAPI, **A, B**: *blue*; **C, D**: *gray*) of cell types associated with blood vessels. (**E**) Immunofluorescent labeling of EM48 (*red*) also revealed the co-localization of mHtt+ aggregates within small blood vessels labeled with the endothelial marker CD31 (*green*). Abbreviations: α-SMA: alpha-smooth muscle actin; DAPI: 4', 6-diamidino-2-phenylindole. Scale bars **A, B** = 30 µm; **C, D** = 25 µm; **E** = 50 µm; **E',E"** = 25 µm.

Figure 3. Morphological changes in blood vessels in mild-to-moderate stage HD patients. (**A-C**) aCBV and (**A**) arterial transit time (**B**) quantifications (*n*=8 HD; *n*=7 CTL) as well as maps (**C**) of a representative HD subject for each of the 3 slices acquired. Scale in (**C**) represent the amount of ml blood/ml tissue. The caudate nucleus ROI is delineated in *blue* and the putamen ROI in *green*. (**D**) Brain angiograms, as acquired using 7T MRI of a representative HD patient and a matched control. Data are expressed as means ± SEM. Statistical analysis was performed using a paired Student's *t*-test. * $p<0.05$ as compared to controls. Abbreviations: Ant: anterior; CTL: controls; L: left; HD: Huntington's disease; Post: posterior; R: right.

Figure 4. Morphological changes in blood vessels in post-mortem brain samples of HD patients. (**A**) Increase in blood vessel density in the HD putamen (*n*=24) as compared to controls (*n*=9). (**B**) Collagen IV immunofluorescent staining (*green*) revealed an increase in the density of blood vessels in the putamen of an HD case, as well as the matching black-and-white masks used for blood vessel measurements. (**C**) Positive correlation of blood vessel density and putaminal atrophy in HD patients. (**D**) Quantification of the blood vessel diameter of small- and medium-sized blood vessels did not reveal any differences in diameter, but uncovered an increase in the proportion of small blood vessels (5-10 µm) and a decrease in the proportion of larger-calibre blood vessels (10-20 µm) in the HD putamen (**E**). Average size (**F**) and average Feret diameter (**G**) positively correlate with the surface area of the putamen. (**H**) Wall thickness of small (5-10 µm) and larger-calibre blood vessels (10-20 µm) does not differ from controls. Data are expressed as Means ± SEM. Statistical analysis was performed using an ANCOVA with age and gender as covariates followed by a Bonferroni post-hoc test. Coefficients of correlation were determined using the Pearson's correlation test. * $p<0.05$, ** $p<0.01$ vs. controls. Abbreviations: CTL: controls; L: left; HD: Huntington's disease. Scale bar **B** = 100 µm.

Figure 5. Morphological changes in striatal blood vessels of R6/2 mice. (**A**) Increase in blood vessel density in the striatum of 12-week old R6/2 mice (*n*=9) as compared to WT littermates (*n*=9). (**B**) Striatal collagen IV immunofluorescent staining (*green*) depicting an increase in density of blood vessels in the striatum of R6/2 mice as well as the matching black-and-white masks used

for blood vessel measurements. (**C**) Quantification of the average size of striatal blood vessels revealed a decrease in R6/2 mice (*n*=9) as compared to WT littermates (*n*=9). (**D**) No difference was observed in the size of arterioles nor capillaries-venules in R6/2 mice (*n*=6) as compared to WT littermates (*n*=6). (**E, F**) Scanning electron microscopy depicting decreases in the size of blood vessel branching (*white* arrowheads) and presence of unformed, blind-ending branches (*blue* arrowhead) in the striatum of R6/2 mice. (**G**) Quantification of striatal vascular network volume and vascular network surface area using *in situ* cerebral perfusion with [^{14}C]sucrose and [^{3}H]diazepam did not detect differences between WT (*n*=9) and R6/2 mice (*n*=9). Data are expressed as means ± SEM. Statistical analysis was performed using an unpaired Student's *t*-test, with application of a Welch correction in cases of unequal variances. * $p<0.05$, ** $p<0.01$ vs. controls. Abbreviations: WT: wild type. Scale bars **B** = 100 µm; **E** = 25 µm, except bottom left image = 100 µm.

Figure 6. Post-mortem evidence of BBB disruption in HD patients. (**A**) Western blot measurements of the TJ proteins claudin-5 and occludin revealed a significant decrease of both proteins in the putamen of HD patients (*n*=24) as compared to controls (*n*=13). (**B**) Method used for the quantification of the extravascular fibrin staining. A *yellow* mask of the fibrinogen staining and a *magenta* mask of the collagen IV staining were generated using Image J and merged using Adobe Photoshop. The *magenta and white* (from merging magenta and yellow) were then deleted, leaving only the extravascular fibrinogen staining (*yellow*), the surface area of which was quantified for each sample using image J. (**C**) Quantification of the extravascular fibrin positive staining shows an increase in fibrin levels outside the blood vessels in the putamen of HD patients (*n*=8) compared to controls (*n*=5). (**D**) Expression of protein markers associated with increased BBB permeability and angiogenesis was assessed using a multiplex ELISA assay in the human putamen of HD patients (*n*=24) and matched controls (*n*=14). Statistical analyses were performed using an ANCOVA with age and sex as covariates, followed by a Bonferroni post-hoc test. * $p<0.05$, ** $p<0.01$, *** $p<0.001$ as compared to controls. Abbreviations: CTL or C: controls; Coll IV: collagen IV; HD or H: Huntington's disease. . Scale bar **C** = 100 µm.

Figure 7. *In vivo* evidence of BBB disruption in HD patients. (**A**) Quantification of Gd-DTPA in the caudate and putamen of HD patients (*n*=7) and age- and sex-matched controls (*n*=7). (**B**) Brain map of Gd-DTPA leakage from a representative HD patient and a control, with ROI for the left and right caudate and putamen (*white*) (**C**) BBB permeability in the right caudate nucleus positively correlated with the burden of disease score in HD patients, although all regions showed a similar trend. Statistical analysis was performed using a paired Student's *t*-test. Coefficients of correlation were determined using the Pearson's correlation test; * $p<0.05$. Abbreviations: CTL: controls; HD: Huntington's disease.

Figure 8. Evidence of paracellular disruption of the BBB in the R6/2 mouse. (**A-C**) Transmission electron microscopy in the striatum of R6/2 mice (*n*=6) showing wider intercellular clefts of TJs (*white* arrowheads, in **C**) on the lumenal side (**A**) as well as a wider angle of TJs with respect to the lumen as compared to WT littermates (*n*=6) (**B**). (**C**) Representative transmission electron micrographs of a TJ in a WT and a R6/2 mouse. (**D**) Measurements of the expression of the TJ proteins claudin-5 and occludin reveal a significant decrease of both proteins in the R6/2 striatum (*n*=8) as compared to WT (*n*=7). (**E**) A greater number of CD45+ perivascular macrophages (*gray*) are associated with blood vessels (collagen IV; *red*) in the R6/2 mouse as compared to WT. Data are expressed as means ± SEM. Statistical analysis was performed using an unpaired Student's *t*-test, with a Welch correction if variances were not equal. * $p<0.05$ vs. controls. Abbreviations: Coll IV: collagen IV; DAPI: 4', 6-diamidino-2-phenylindole; L: lumen; TJ: tight junction; WT: wild type. Scale bars **C** = 100 nm; **E** = 30 µm.

Figure 9. Evidence for disruption of transcytosis in the R6/2 mouse. (**A**) Quantification of the mean vesicle density with increases in R6/2 mice. (B) Examples of luminal vesicle type I (*red* arrowhead), type II (*white* arrow), cytoplasmic (*white* arrowhead) and abluminal vesicles (*red* arrow) depicted by transmission electron microscopy. (**C**) Quantification of the different types of vesicles revealed an increase in total vesicles and in type II luminal vesicles in R6/2 mice. (**D**) mHtt aggregates were detected using EM48 immunogold labeling in the endothelium of R6/2 mice (inset 3) as well as in luminal type I (insets 1, 2 and 5), type II (inset 6), cytoplasmic (inset 8) and

abluminal vesicles (inset 4). Gold particles were also frequently found in pericytes of R6/2 mice (inset 7). (**E**) Quantification of albumin+ staining (*green*) reveals an increase of albumin in the striatal parenchyma of R6/2 mice (*n*=8) as compared to WT littermates (*n*=5). Blood vessels were stained using lectin-594 (*red*). (**F**) Transmission electron microscopy analysis of pericyte coverage did not unveil any difference between R6/2 (*n*=6) and WT littermates (*n*=6). (**G**) qPCR quantification of PDGFβ in the mouse striatum showed a decrease in R6/2 mice (*n*=10) as compared to WT (*n*=10). Data are expressed as means ± SEM. Statistical analysis was performed using an unpaired Student's *t*-test, with a Welch correction when variances were unequal. * $p<0.05$, ** $p<0.01$ as compared to controls. Abbreviations: E: endothelium; L: lumen; PDGFβ: platelet-derived growth factor β; WT: wild type. Scale bars **B** = 100 nm; **D** = 200 nm; **E** = 100 µm.

Figure 10. Schematic recapitulating findings collected both in R6/2 and HD patients as well as the hypothesized transport of mHtt to the brain by the transmigration of immune cells through the leaky BBB.

Table 1

3T MRI-DCE									
	Age	**Sex**	**CAG**	**Disease duration**	**UHDRS**	**TFC**		**Age**	**Sex**
Patients	41	M	43	nk	0	12	**Controls**	27	M
	42	F	44	nk	13	9		37	F
	49	M	43	11	18	5		38	M
	51	M	43	14.5	3	12		39	M
	59	F	41	24.5	30	6		52	M
	66	M	42	5	12	13		55	F
	68	M	41	13.5	18	11		63	M

7T MRI ASL									
	Age	**Sex**	**CAG**	**Disease duration**	**UHDRS**	**TFC**		**Age**	**Sex**
Patients	27	M	nk	6	38	5	**Controls**	28	M
	51	M	43	11	18	5		47	M
	51	M	43	14	16	11		53	M
	60	F	41	25	30	6		54	M
	63	M	nk	22	32	1		61	M
	65	M	42	7	12	13		63	F
	67	M	41	13	18	11		64	M
	77	M	30	10	15	7			

Figure 1

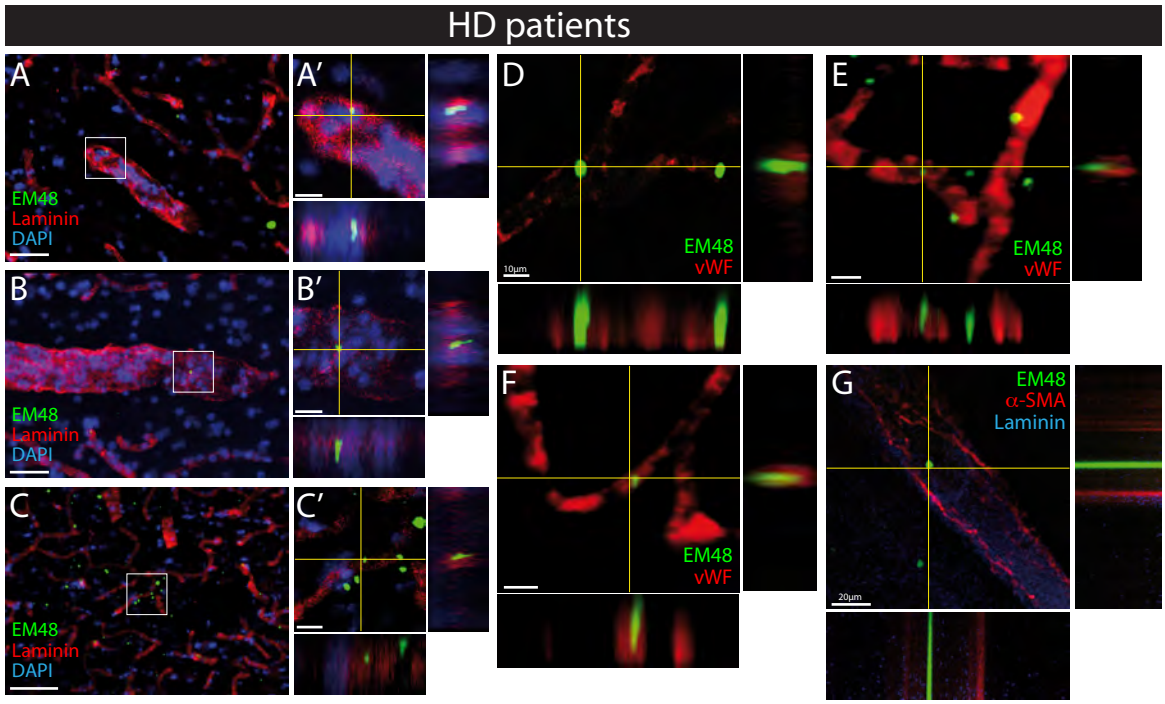
HD patients
A
A′
B
B′
C
C′
D
E
F
G
EM48
Laminin
DAPI
EM48
vWF
EM48
α-SMA
Laminin
10µm
20µm

Figure 2

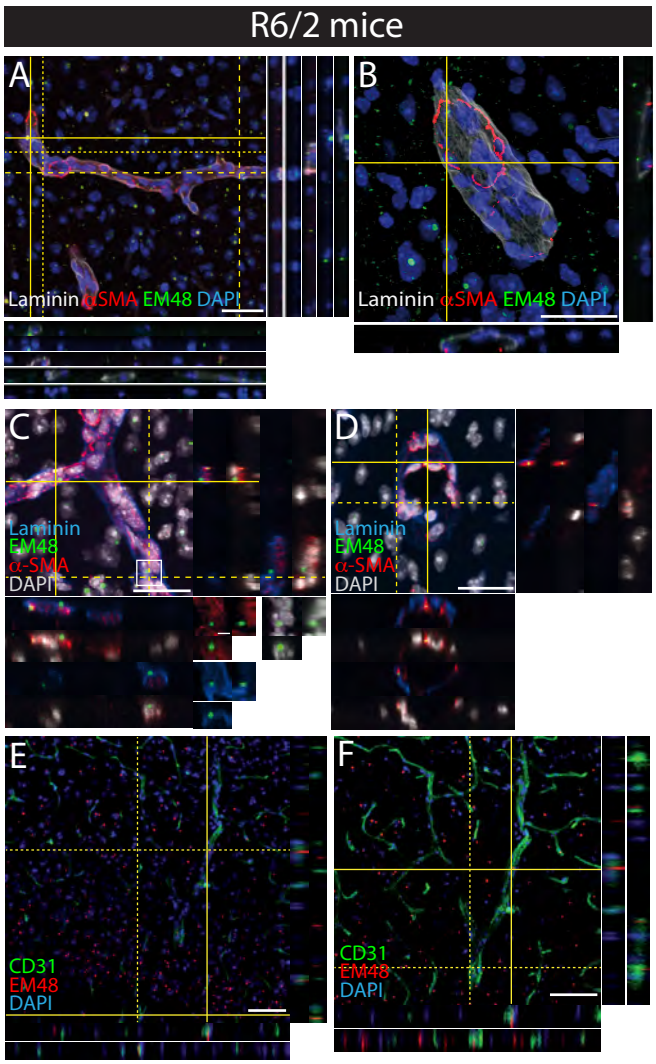
R6/2 mice
A
Laminin αSMA EM48 DAPI
B
Laminin αSMA EM48 DAPI
C
Laminin
EM48
α-SMA
DAPI
D
Laminin
EM48
α-SMA
DAPI
E
CD31
EM48
DAPI
F
CD31
EM48
DAPI

Figure 3

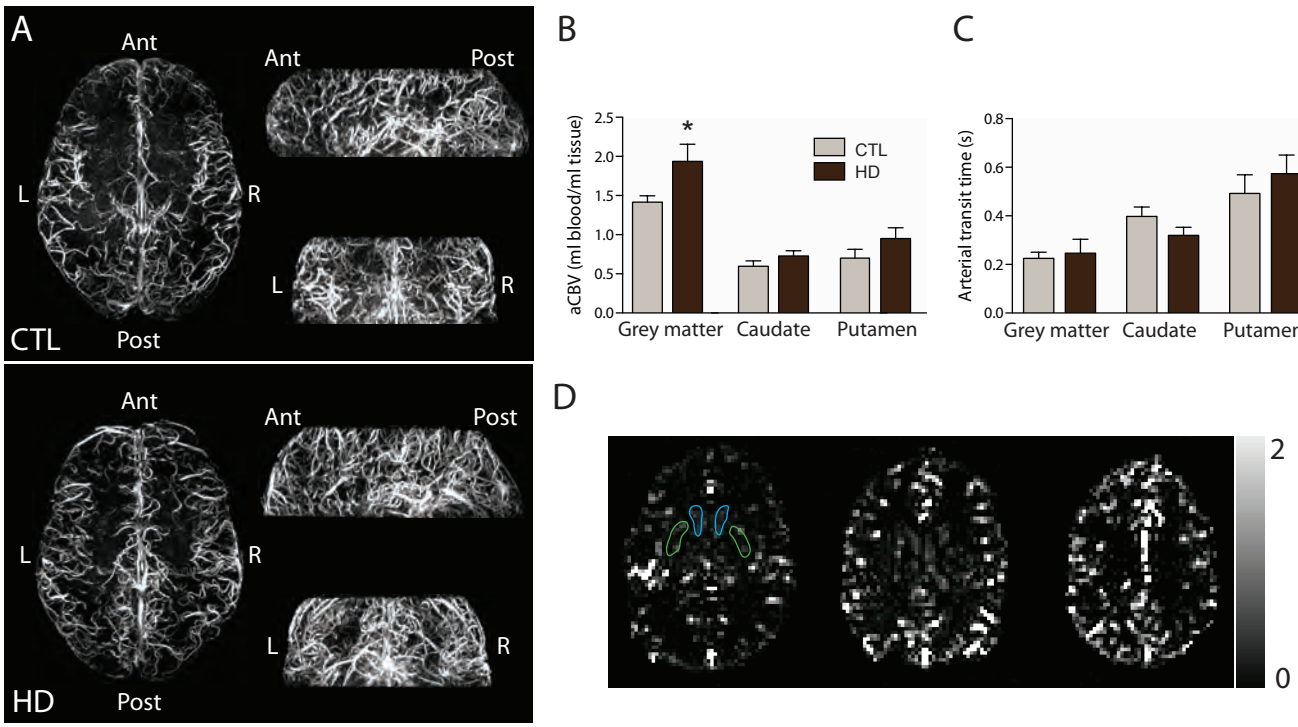
A
Ant
Ant
Post
L
R
L
R
CTL
Post
Ant
Ant
Post
L
R
L
R
HD
Post
B
aCBV (ml blood/ml tissue)
2.5
2.0
1.5
1.0
0.5
0.0
*
CTL
HD
Grey matter
Caudate
Putamen
C
Arterial transit time (s)
0.8
0.6
0.4
0.2
0.0
Grey matter
Caudate
Putamen
D
2
0

Figure 4

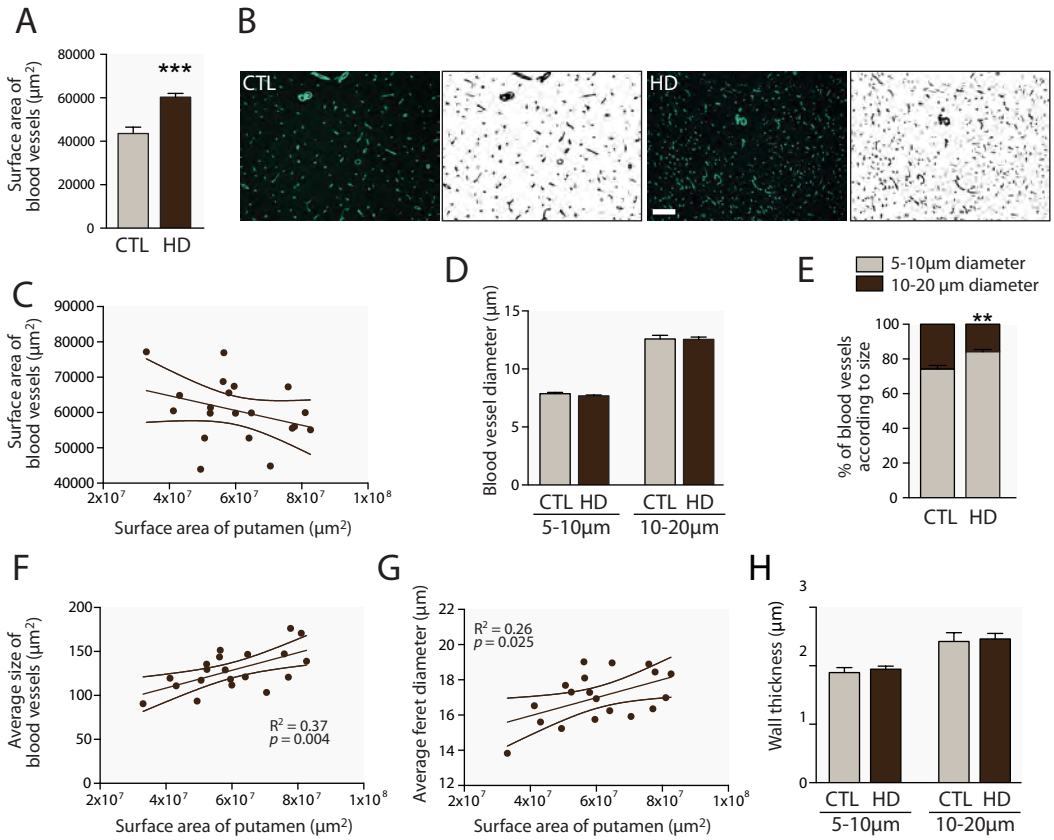
A
B
C
D
E
F
G
H
Surface area of blood vessels (µm²)
***
CTL
HD
Surface area of putamen (µm²)
Blood vessel diameter (µm)
5-10µm diameter
10-20 µm diameter
% of blood vessels according to size
**
Average size of blood vessels (µm²)
R² = 0.37
p = 0.004
Average feret diameter (µm)
R² = 0.26
p = 0.025
Wall thickness (µm)
5-10µm
10-20µm

Figure 5

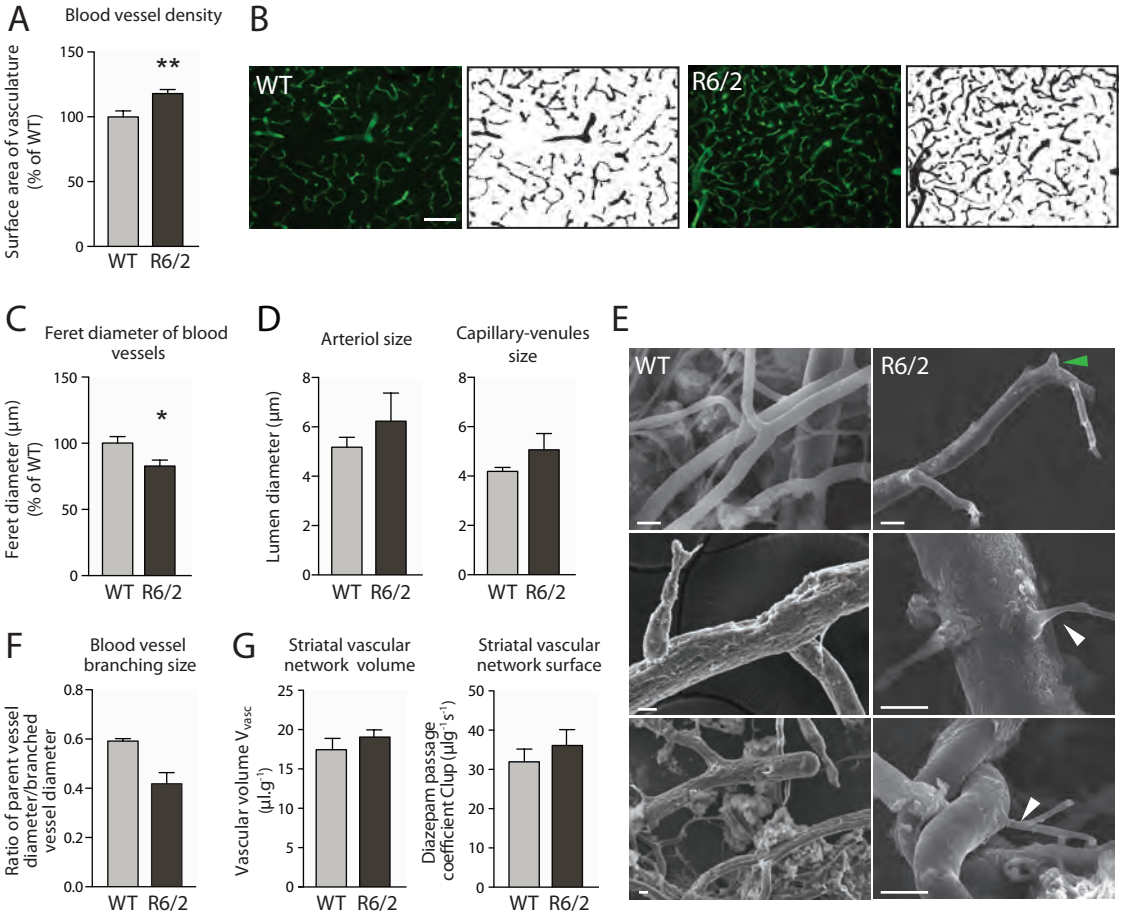
A
Blood vessel density
Surface area of vasculature (% of WT)
150
100
50
0
**
WT R6/2
B
WT
R6/2
C
Feret diameter of blood vessels
Feret diameter (µm) (% of WT)
150
100
50
0
*
WT R6/2
D
Arteriol size
Lumen diameter (µm)
8
6
4
2
0
WT R6/2
Capillary-venules size
8
6
4
2
0
WT R6/2
E
WT
R6/2
F
Blood vessel branching size
Ratio of parent vessel diameter/branched vessel diameter
0.8
0.6
0.4
0.2
0.0
WT R6/2
G
Striatal vascular network volume
Vascular volume V_{vasc} (µl.g^{-1})
25
20
15
10
5
0
WT R6/2
Striatal vascular network surface
Diazepam passage coefficient Clup (µlg^{-1}s^{-1})
50
40
30
20
10
0
WT R6/2

Figure 6

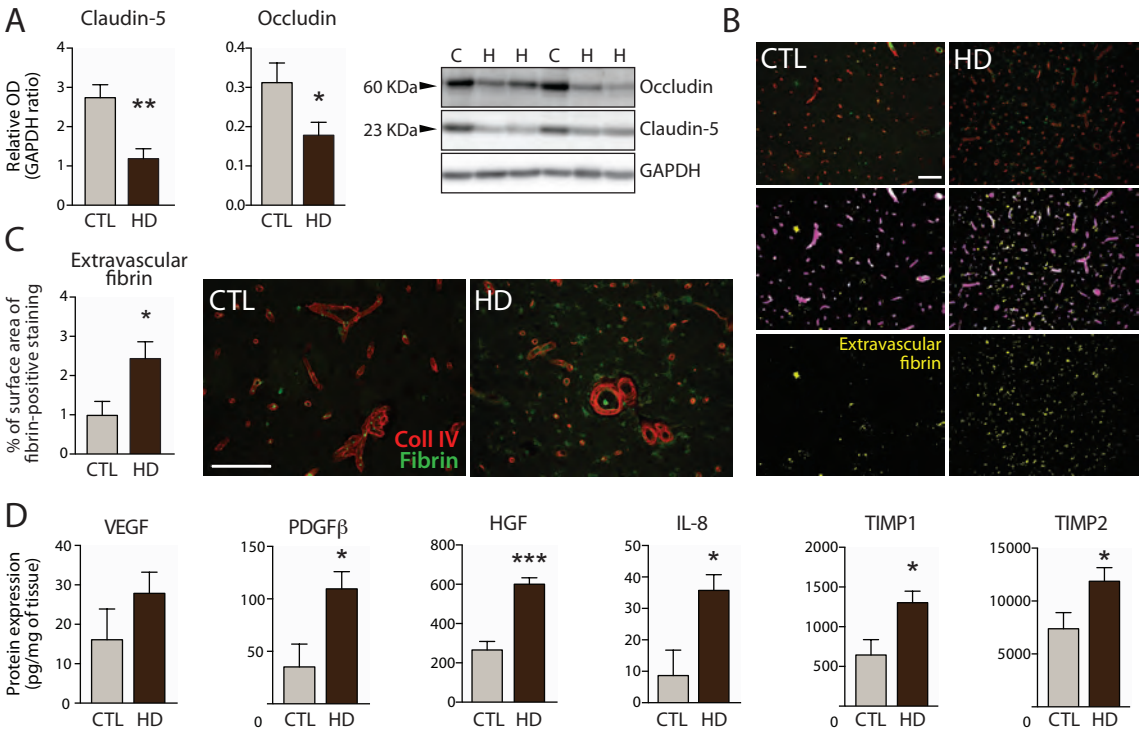
A
Claudin-5
Occludin
Relative OD (GAPDH ratio)
CTL HD
C H H C H H
60 KDa
23 KDa
Occludin
Claudin-5
GAPDH
B
CTL
HD
Extravascular fibrin
C
Extravascular fibrin
% of surface area of fibrin-positive staining
Coll IV
Fibrin
D
VEGF
PDGFβ
HGF
IL-8
TIMP1
TIMP2
Protein expression (pg/mg of tissue)

Figure 7

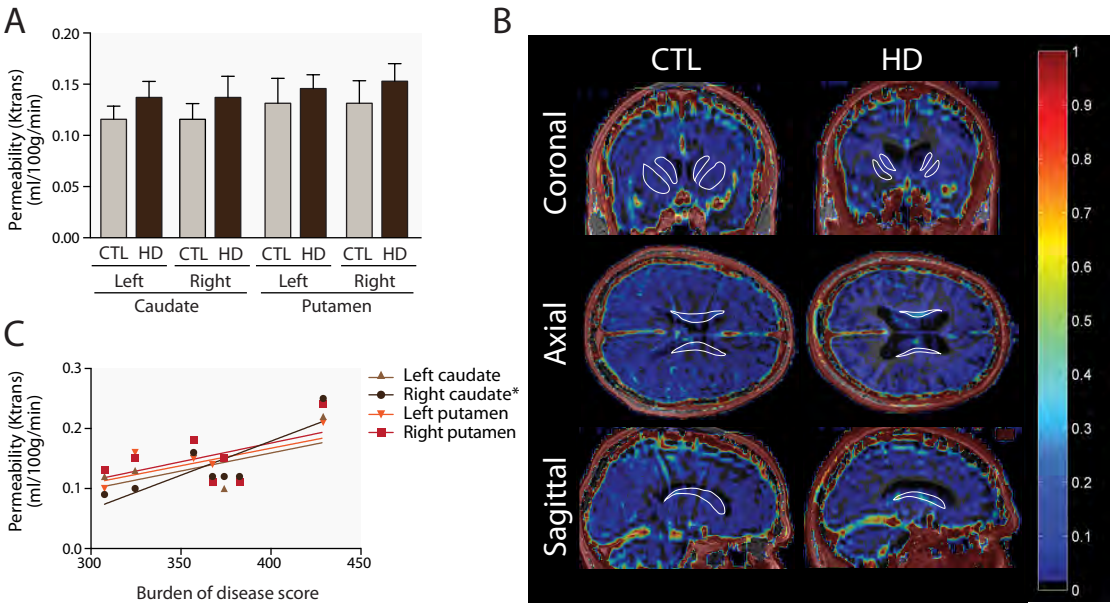
A
Permeability (Ktrans) (ml/100g/min)
0.20
0.15
0.10
0.05
0.00
CTL HD CTL HD CTL HD CTL HD
Left Right Left Right
Caudate Putamen
B
CTL
HD
Coronal
Axial
Sagittal
1
0.9
0.8
0.7
0.6
0.5
0.4
0.3
0.2
0.1
0
C
Permeability (Ktrans) (ml/100g/min)
0.3
0.2
0.1
0.0
300
350
400
450
Burden of disease score
Left caudate
Right caudate*
Left putamen
Right putamen

Figure 8

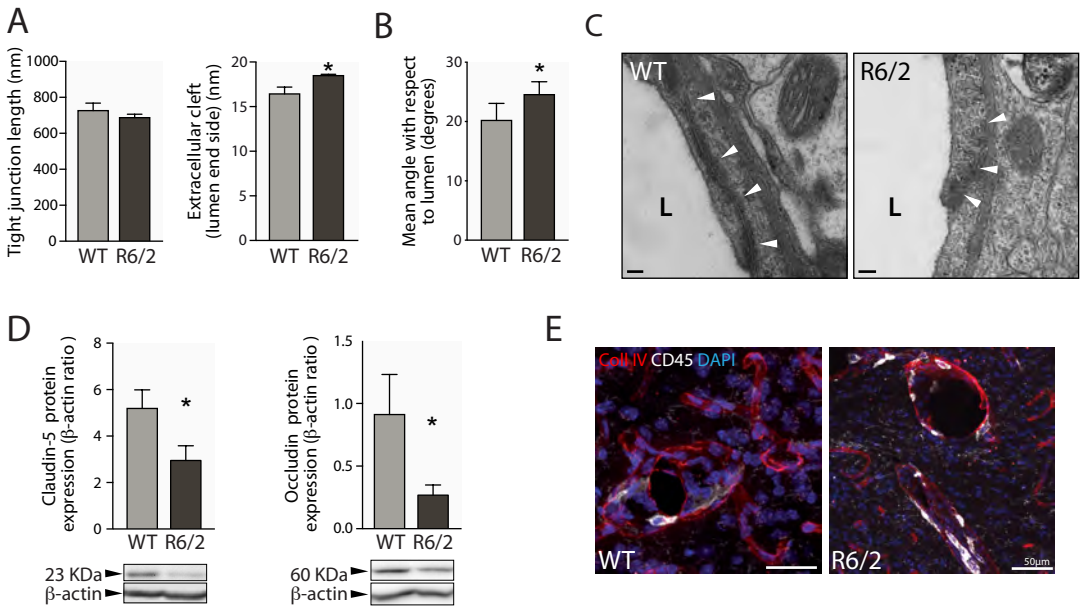
A
Tight junction length (nm)
1000
800
600
400
200
0
WT R6/2
Extracellular cleft (lumen end side) (nm)
20
15
10
5
0
*
WT R6/2
B
Mean angle with respect to lumen (degrees)
30
20
10
0
*
WT R6/2
C
WT
L
R6/2
L
D
Claudin-5 protein expression (β-actin ratio)
8
6
4
2
0
*
WT R6/2
23 KDa
β-actin
Occludin protein expression (β-actin ratio)
1.5
1.0
0.5
0.0
*
WT R6/2
60 KDa
β-actin
E
Coll IV CD45 DAPI
WT
R6/2
50μm

Figure 9

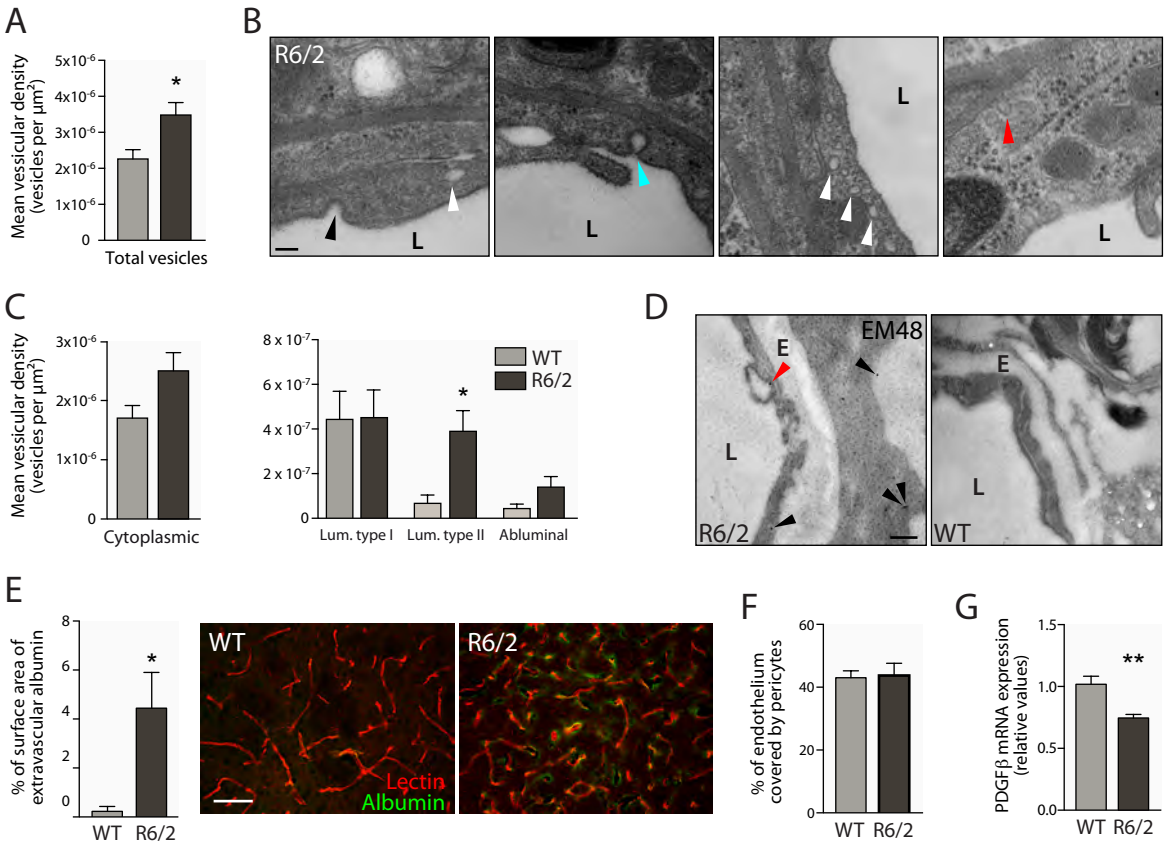
A
Mean vessicular density (vesicles per µm²)
5x10⁻⁶
4x10⁻⁶
3x10⁻⁶
2x10⁻⁶
1x10⁻⁶
0
*
Total vesicles
B
R6/2
L
L
L
L
C
Mean vessicular density (vesicles per µm²)
3x10⁻⁶
2x10⁻⁶
1x10⁻⁶
0
Cytoplasmic
8 x 10⁻⁷
6 x 10⁻⁷
4 x 10⁻⁷
2 x 10⁻⁷
0
WT
R6/2
*
Lum. type I
Lum. type II
Abluminal
D
EM48
E
L
R6/2
E
L
WT
E
% of surface area of extravascular albumin
8
6
4
2
0
*
WT
R6/2
WT
R6/2
Lectin
Albumin
F
% of endothelium covered by pericytes
60
40
20
0
WT
R6/2
G
PDGFβ mRNA expression (relative values)
1.5
1.0
0.5
0.0
**
WT
R6/2

Suppl Table 1

	ID	GRADES	age	sex	CAG repeats	PM delay
HD cases	**H689**	1	73	M	nk	nk
	H681	2	64	M	45	nk
	H697	2	45	M	47	nk
	H704	2	57	M	43	2.3
	H706	2	66	M	46	30.3
	H711	2	73	M	45	33
	H721	2	61	M	46	29
	H630	3	63	M	46	nk
	H646	3	59	M	46	73
	H652	3	34	M	47	nk
	H653	3	65	F	44	nk
	H685	3	47	M	49	nk
	H688	3	54	M	47	nk
	H690	3	55	M	51	26
	H696	3	61	F	46	nk
	H701	3	51	M	49	14.3
	H712	3	78	M	43	29
	H714	3	63	F	46	42.3
	H722	3	73	M	45	35
	H644	4	51	M	52	24
	H674	4	53	F	52	nk
	H682	4	40	M	51	nk
	H683	4	47	M	52	30
	H684	4	50	M	50	nk
	H687	4	43	M	53	nk
	H691	4	65	M	46	nk
	H692	4	43	F	54	nk
	H693	4	26	F	70	42.3
	H708	4	44	M	53	30.3
	H710	4	43	M	51	40.3
	H720	4	68	M	45	nk
Control cases	**C515**		54	M		nk
	C518		40	M		nk
	C541		61	F		nk
	C547		72	F		nk
	C557		61	M		28.2
	C566		56	M		22
	C567		75	M		17
	C568		69	M		55
	C572		59	M		30
	PT114		63	F		72
	PT34		61	F		71
	PT51		67	M		14.3
	PT56		67	M		29.3
	PT62		78	M		77
	S177		59	M		nk
	Y36		32	M		nk